Simultaneous normal and torsional force measurement by cantilever surface contour analysis

2011 Meas. Sci. Technol. 22 055103

(http://iopscience.iop.org/0957-0233/22/5/055103)

Meas. Sci. Technol. **22** (2011) 055103 (11pp) doi:10.1088/0957-0233/22/5/055103

Simultaneous normal and torsional force measurement by cantilever surface contour analysis

Lee Kumanchik[1], **Tony Schmitz**[1,3] **and Jon Pratt**[2]

[1] Department of Mechanical and Aerospace Engineering, University of Florida, Gainesville, FL, USA
[2] Physical Measurement Laboratory, National Institute of Standards and Technology, Gaithersburg, MD, USA

E-mail: leemk@ufl.edu, tschmitz@ufl.edu and jon.pratt@nist.gov

Received 9 November 2010, in final form 7 March 2011
Published 8 April 2011
Online at stacks.iop.org/MST/22/055103

Abstract
This study presents an alternative to the current Hooke's law-based force relation between rectangular cantilever deflection and applied force. In the new approach, a transduction constant is presented that (1) includes no cross-talk between torsion and normal force components, (2) is independent of the load application point, and (3) does not depend on the cantilever beam length. Rather than measuring the cantilever deformation at a single point (such as the tip location), it is measured at multiple adjacent points using scanning white light interferometry to provide a three-dimensional description of the cantilever deformation during loading. This measurement, processed by a force relation based on a superposition of deflections derived from Euler–Bernoulli bending theory and St Venant's torsion theory, provides the vertical, axial, and torsional force components simultaneously. Experimental results are compared to force predictions for the vertical and torsional components using macro-scale cantilevers under mass loading. An uncertainty analysis is also provided.

Keywords: microscopy, force, atomic, interferometry, stiffness, calibration

(Some figures in this article are in colour only in the electronic version)

1. Introduction

The atomic force microscope (AFM) is an instrument that uses an elastically deformable cantilever with a specialized tip, or stylus, as a mechanical probe. The cantilever deformation, monitored by a detector, is used to infer the tip-to-sample interaction forces. Although the entire cantilever deforms, the detector typically only determines the motion at or near the tip (located at the free end of the cantilever). This is a natural choice since the AFM can perform imaging with the tip motion having a one-to-one correlation (ideally) to a sample's surface contours. When used for force measurement, Hooke's law, $F = ky$, is used, where it is assumed that F is the vertical force, k is the cantilever bending stiffness, and y is the vertical tip motion. A schematic is included in figure 1 to identify the cantilever deformation due to a single point on the sample surface; the reader will note that this simple representation does not capture the actual geometry of typical AFMs.

The AFM has become ubiquitous in the research setting. It is commonly used in ultramicroscopy (imaging at atomic resolution) since it can be applied to non-conducting samples. Some example applications include biological by Franz and Puech (2008), crystalline growth by Kalb *et al* (2004), and pharmaceutical drug imaging by Veerapandian and Yun (2009). However, the AFM is not restricted to imaging. It is also used in atomic scale manipulation by Custance *et al* (2009), nanolithography by Rosa and Liang (2009), and data storage and retrieval, such as IBM's Millipede project by Vettiger *et al* (2002). The AFM has also become a potential tool for quality control in microelectromechanical systems (MEMS) as a parallel technique to electronic quality control in microchip manufacturing; see Liu and Bhushan (2004).

[3] Author to whom any correspondence should be addressed.

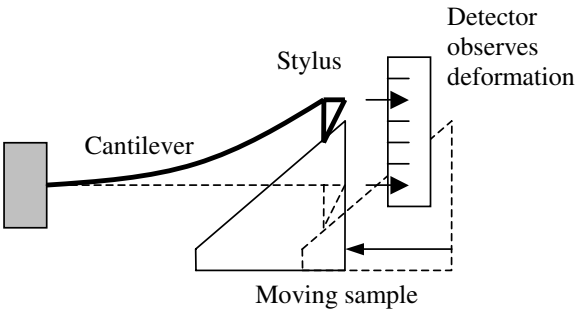

Figure 1. Simple schematic of AFM operation. Stylus forces cause deformation of the cantilever and a detector observes the deformation at a single point.

This is due to the AFM's force measuring capabilities, which enable material and mechanical testing. Many fields can benefit from the AFM's ability to measure micro-scale forces. For example, there are efforts to measure the bonding forces between complementary nucleotides in DNA by Bornschlog and Rief (2008) and the mechanical stability of proteins has also been tested by Brockwell (2007). In tribology, the AFM is used to measure friction, such as between microspheres by Ling *et al* (2007) and in capillary force analysis by Butt and Kappl (2009).

Due to the AFM's popularity as a multi-function instrument, vendors strive for 'turn-key' system operation. However, achieving good force accuracy under this paradigm can be challenging. For example, cantilever stiffness studies have found that the manufacturer-specified stiffness can vary by as much as 300% from the calibrated value; see Langlois *et al* (2007). One study by Emerson and Camesano (2006) combined all manufacturer specifications required for force measurement (including stiffness) and found that the combined uncertainty was greater than 1500%. While this level of divergence may not always be present, calibrating the AFM is clearly required to obtain meaningful results. However, after decades of calibration research, the best stiffness calibrations, performed by international standards agencies, are accurate to a few percent as described by Kim and Pratt (2010). Using methods available to the average user, the accuracy of stiffness calibration, in general, is limited to a range of 10–20% as reported by Emerson and Camesano (2006) and Matei *et al* (2006). Because stiffness is one of the parameters required to determine force, the accuracy of the force measurement will be no better than the stiffness accuracy and, most likely, will be worse.

A more fundamental limitation is the assumed force relation, $F = ky$. Cantilever mechanics studies by Heim *et al* (2004) have shown how cross-axial sensitivity to forces perpendicular to the measurement direction leads to a systematic error between 10% and 20%. This error is independent of stiffness and displacement calibration. Other force relations have been proposed which take into account forces that arise from contact mechanics at the cantilever's tip. These have attempted to capture tip geometry (Kopycinska-Müller *et al* 2006), elastic deformation of the sample (VanLandingham *et al* 1997), cantilever inclination angle (Heim *et al* 2004), adhesion (Sarid *et al* 1998), and friction (Karhu *et al* 2009, Ogletree *et al* 1996). These compensatory post-processing techniques are largely unused for several reasons. First, their complexity requires expertise in mechanics to understand and programming knowledge to implement. Second, they require geometrical parameters of the AFM setup (which are difficult to obtain) and knowledge of the tip-to-sample contact mechanics (often unknown *a priori*). Third, the models are highly situational. For example, if the sample is very hard, plastic deformation is unlikely to occur or, if the cantilever and sample are submerged in water, capillary force is mitigated. Also, some are updated every few years leading to extra effort for users to stay current; see Heim *et al* (2004), Wang (2009), Hutter (2005), and Edwards *et al* (2008). Therefore, the simple force relation, $F = ky$, remains in use. In a comprehensive review (1254 cited references) of AFM calibration and implementation in numerous fields by Butt *et al* (2005), there was no mention of an alternative force relation to $F = ky$.

Given the existing limitations, an alternative, yet simple, force relation with a transduction constant that is easier to calibrate than stiffness and that has no cross-axial sensitivity is desired. This paper details a new method for determining force that achieves these goals. The advantages of this method are that it includes no cross-talk between torsion and normal force components, is independent of the load application point, and does not depend on the rectangular cantilever beam length. Rather than measuring the cantilever deformation at a single point (such as the tip location), it is measured at multiple points to provide a three-dimensional description of the cantilever deformation. This measurement, processed by an alternative force relation, provides the vertical, axial, and torsional force components simultaneously (the vertical and torsional components predictions are experimentally verified in this study). The paper is organized as follows. First, the force model and experimental setup are described. Second, the model is evaluated using large-scale (macro) cantilevers. While these macro-scale cantilevers do not represent the micro-scale geometry of traditional AFM probes, it enables the proof-of-concept for the new force relation to be conveniently demonstrated. An uncertainty analysis based on the experimental setup is provided. Third, conclusions and future work, including the extension of this work to the micro-scale, are discussed.

2. Three-dimensional force relation

The three-dimensional elastic response of a cantilever due to an arbitrary force applied at the stylus can be approximated by combining two elasticity theories: (1) Euler–Bernoulli beam bending theory to describe deformation by forces applied on the x–y plane that cause bending; and (2) St Venant's torsion theory to describe deformation by forces applied in the y–z plane that cause twist. For small deformations, these two contributions can be superimposed to provide an analytical description for the three-dimensional deformation of the cantilever to an arbitrary force. Figure 2 shows the cantilever, axis directions, and three components of an

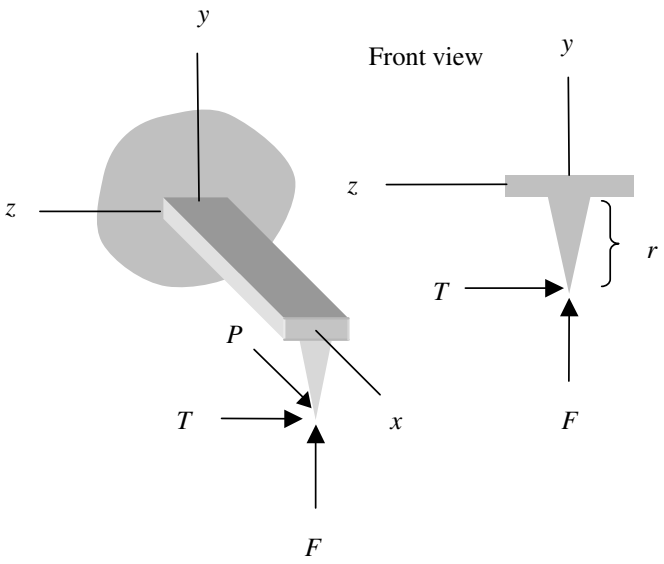

Figure 2. Arbitrary force applied to a cantilever at the stylus with components F, P, and T.

arbitrary force: F for the vertical, or normal, force; P for the axial force; and T for the torsion force.

The general Euler–Bernoulli beam bending equation is

$$\frac{\partial^2}{\partial x^2}\left(EI\frac{\partial^2 y}{\partial x^2}\right) = u, \tag{1}$$

where x is the distance along the beam axis, y is the deformation perpendicular to the beam axis, E is the modulus of elasticity, I is the second moment of area, and u is a distributed load. Assuming that $y = y(x)$, $u = 0$, fixed–free boundary conditions, and EI is constant, integration is straightforward and yields four equations:

$$EI\frac{\partial^3 y}{\partial x^3} = C_1 = -F \tag{2}$$

$$EI\frac{\partial^2 y}{\partial x^2} = C_1 x + C_2 = M(x) \tag{3}$$

$$EI\frac{\partial y}{\partial x} = C_1\frac{x^2}{2} + C_2 x + \overset{=0}{C_3} \tag{4}$$

$$EIy(x) = C_1\frac{x^3}{6} + C_2\frac{x^2}{2} + C_3 x + \overset{=0}{C_4}, \tag{5}$$

where (2) is balanced with shear force, (3) is balanced with moment, and the integration constants C_3 and C_4 are zero due to the rigid boundary condition at the fixed end (base) of the cantilever. Solving for the remaining coefficients yields the deformation equation

$$y(x) = \frac{-F}{6EI}x^3 + \frac{FL + Pr}{2EI}x^2, \tag{6}$$

where L is the cantilever length and r is the stylus height.

St Venant's torsion theory states that the rate of twist is proportional to the applied torque:

$$GJ\frac{\mathrm{d}\alpha}{\mathrm{d}x} = \mathrm{Tr}, \tag{7}$$

where α is the angular twist about the beam axis, G is the shear modulus, and J is the torsion constant. Integrating once and converting from angular twist to deflection ($\alpha z \approx y$) yields

$$GJy(x, z) = \mathrm{Tr}\,xz + \overset{=0}{C_5}\,z, \tag{8}$$

where z is the location across the width of the beam and C_5 is zero due to the rigid boundary condition at the cantilever base. The resulting deformation equation is

$$y(x, z) = \frac{\mathrm{Tr}}{GJ}xz. \tag{9}$$

Combining the two deformation equations, (6) and (9), yields

$$\begin{aligned} y(x, z) &= \frac{-F}{6EI}x^3 + \frac{FL + Pr}{2EI}x^2 + \frac{Tr}{GJ}xz \\ &= B_3x^3 + B_2x^2 + B_1xz, \end{aligned} \tag{10}$$

where B_1, B_2, and B_3 generalize the deformation equation. Equation (10) analytically describes the three-dimensional deformation of a cantilever under an arbitrary load applied at the stylus[4] . As discussed previously, a single measurement of y is traditionally performed at an ideally known point x to determine the force at the stylus. By the analysis presented here, there are clearly more unknowns than equations and a unique solution is obtained only by making additional assumptions about the nature of the contact mechanics based on the properties of the measurement environment. In this research, measurements are performed at multiple (x, y, z) locations simultaneously rather than just a single point. The corresponding system of equations in matrix form is

$$\begin{bmatrix} x_1^3 & x_1^2 & x_1z_1 \\ \vdots & \vdots & \vdots \\ x_n^3 & x_n^2 & x_nz_m \end{bmatrix}_{(n\times m)\times 3} \begin{Bmatrix} B_3 \\ B_2 \\ B_1 \end{Bmatrix}_{3\times 1} = \begin{Bmatrix} gy_1 \\ \vdots \\ y_{n\times m} \end{Bmatrix}_{(n\times m)\times 1}, \tag{11}$$

where m is the number of measurements across the width of the cantilever, n is the number of measurements down the length of the cantilever, and $n \times m$ is the total number of measurements. This can be compactly written as $[XZ]\{B\} = \{Y\}$ and the coefficients can be determined in a least-squares sense using the pseudo-inverse:

$$\{B\} = [XZ]^+\{Y\}. \tag{12}$$

The force components can then be resolved based on the estimated coefficients using (13) through (15):

$$F = -6EIB_3 \tag{13}$$

$$P = \frac{2EI}{r}(B_2 + 3B_3L) \tag{14}$$

$$T = \frac{GJB_1}{r}. \tag{15}$$

Since no additional assumptions were necessary to obtain the force components, this technique is robust to the measurement environment. Also, the parameters in the force equations become the new transduction constants. For example, in (13), the term $-6EI$ is analogous to stiffness, k, yet it is not

[4] Note that the stylus is assumed to be rigid in this analysis.

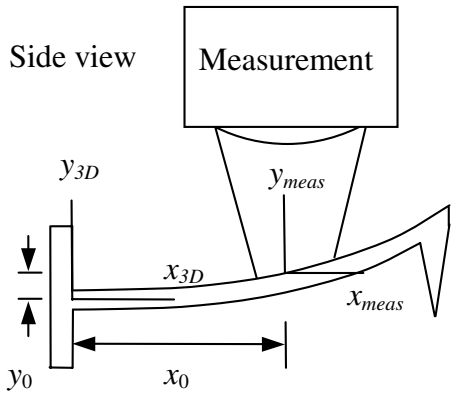

Figure 3. The measurement has its own coordinate system (x_{meas}, y_{meas}, z_{meas}) which is offset from the deformation equation coordinate system (x_{3D}, y_{3D}, z_{3D}) by an unknown amount (x_0, y_0, z_0). The z direction axes are directed out of the page in this view.

dependent on the length of the cantilever, nor is it affected by the contact mechanics[5]. This eliminates some of the challenges currently associated with AFM cantilever stiffness calibration.

In practice, the coordinate system for the measurement does not necessarily coincide with the coordinate system presented in this derivation. Also, it is often the case that the distance between the measurement and derivation coordinate systems is unknown; see figure 3. Therefore, an arbitrary coordinate shift $(x - x_0, y - y_0, z - z_0)$ to the deformation equation is applied. This gives

$$y(x, z) = B_3x^3 + H_1x^2 + H_2x + H_3z + H_4 + B_1xz, \tag{16}$$

where the coefficients H_1 through H_4 are determined by the coordinate shift[6]. The least-squares solution to this new equation follows the same steps as before. Given multiple measurement points (x, y, z), the corresponding system of equations in matrix form is

$$\begin{bmatrix} x_1^3 & x_1^2 & x_1 & z_1 & 1 & x_1z_1 \\ \vdots & \vdots & \vdots & \vdots & \vdots & \vdots \\ x_n^3 & x_n^2 & x_n & z_m & 1 & x_nz_m \end{bmatrix}_{(n\times m)\times 6} \begin{Bmatrix} B_3 \\ H_1 \\ H_2 \\ H_3 \\ H_4 \\ B_1 \end{Bmatrix}_{6\times 1} = \begin{Bmatrix} y_1 \\ \vdots \\ y_{n\times m} \end{Bmatrix}_{(n\times m)\times 1}, \tag{17}$$

which can again be solved in the least-squares sense using the pseudo-inverse as

$$\{BH\} = [XZ]^+ \{Y\}. \tag{18}$$

Naturally, the relationship for P in (14), which includes L, is no longer satisfied, but the relationships for F and T are unaffected so that (13) and (15) still hold. In this research, F and T are quantitatively assessed, while P is left for future work.

3. Experimental description

The multi-point measurement of cantilever deformation was accomplished using a scanning white light interferometer (SWLI) to determine the surface topography of the deflected cantilever. In general, the SWLI detector, a camera, is used to determine a height value, y, for each pixel (after data analysis) and each pixel is given a value, x and z, for its position within the field of view. For the 640 × 480 pixel camera used in this research with the field of view completely filled by a cantilever, there were 307 200 (x, y, z) data points (all results reported here used >200 000 data points). This large dataset was ideal for solving the coefficient matrix in (18) even with many outliers. The SWLI magnification optics chosen for this research gave a field of view of approximately 2.8 mm × 2.1 mm.

A series of macro-scale cantilevers were fabricated from (1 1 1) silicon wafers by diamond cutting through the thickness of the wafers; the plan view dimensions are provided in table 1. The cut direction was selected to fabricate cantilevers with beam axes along the [−1 −1 2] direction. The nominal elastic modulus value for this orientation is $E = 168.9$ GPa (see McSkimin and Andreatch (1964)) and the nominal value for bulk shear modulus is in the range $54.0 \leqslant G \leqslant 64.7$ GPa depending on the cantilever width, w, and thickness, t (see Wortman and Evans (1965)). The moment of inertia and shear rigidity were based on a rectangular cross-section and were computed as $I = \frac{wt^3}{12}$ and $J = \beta wt^3$, respectively, where β is the torsion multiplier (see Srinath (1980)) provided in table 1.

An aluminum 'tee' was fabricated and bonded to the cantilevers using Crystalbond™ heat-activated adhesive[7]; see figure 4. While this tee effectively produced a composite beam (aluminum and silicon with variable cross-section), because the SWLI measurements (figure 3) were performed locally, it was assumed that the mass-loaded tee could be replaced by an equivalent force system that acted on the rest of the silicon cantilever and caused the measured deformation[8]. Although care was exercised in bonding the tee to the cantilevers, the bonding step was manually performed and subject to variability. Therefore, after bonding, the position of the tee's alignment groove was measured relative to the cantilever and used to determine the orientation of the tee (measuring the entire tee required multiple measurements for stitching). The tee had three holes that acted as load points for various masses; see figure 5(*a*). The center hole was for pure bending ($F \neq 0$, $T = P = 0$) and the offset holes were for simultaneous

[5] While often neglected in practice, the stiffness in the traditional force equation $F = ky$ refers to the effective stiffness of the cantilever-to-sample contact, which depends on the specific contact mechanics including, but not limited to, the sample's tribological response.

[6] Rotations were not considered because the cantilevers were leveled during experiments.

[7] Certain commercial equipment, instruments, or materials are identified in the paper in order to specify the experimental procedure adequately. Such identification is not intended to imply recommendation or endorsement by the National Institute of Standards and Technology, nor is it intended to imply that the identified are necessarily the best available for the purpose.

[8] This assumption was based on classic beam mechanics. If a section through the silicon cantilever is defined, then the force/moment combination imposed by the dead weight loads (applied to the tee) is reacted at the section. The deflection response to this force/moment combination is measured by the SWLI.

Table 1. Cantilever geometries. The thickness, t, was approximately 311 μm.

Cantilever number	Length (mm)	Nominal width (mm)	Measured width, w (mm)	Torsion multiplier, β	Positive torque arm (mm)	Negative torque arm (mm)
1	5	1	0.959	0.263	5.339	NA
2	5	1.5	1.454	0.286	5.371	5.605
3	5	2.5	2.462	0.306	5.528	5.448
4	5	3	2.962	0.310	5.355	5.622
5	5	0.7	0.656	0.233	5.221	5.756
6	13	1.5	1.455	0.288	5.378	5.598
7	13	3	2.963	0.310	5.347	5.630
8	13	0.7	0.657	0.233	5.590	5.387

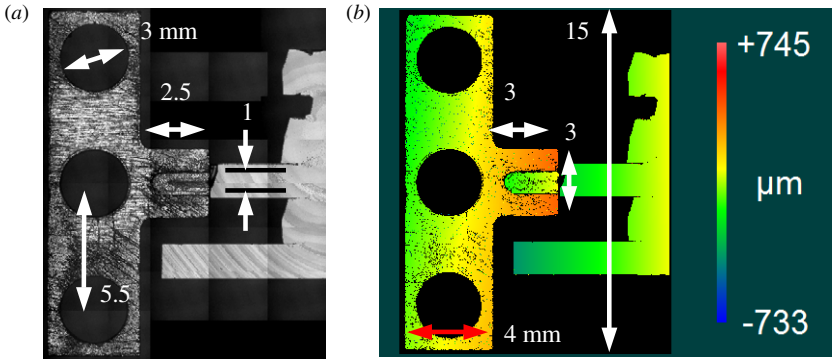

Figure 4. The aluminum 'tee' bonded to a 1.5 mm wide cantilever: (*a*) microscope image of the tee, (*b*) SWLI height map of the tee. Multiple images were stitched together to form these composite images, which enlarged the field of view. The groove near the cantilever was used for alignment purposes.

bending and torsion ($F = T \neq 0$, $P = 0$). The lead masses, shown in figure 5(*b*), were loaded using a ball-in-socket arrangement to control the length of the torque arm; see figure 5(*c*). The torque arms are provided in table 1 and were corrected based on the tee orientation (positive torque arms indicate counter-clockwise twist and negative torque arms indicate clockwise twist).

The experimental procedure was composed of the following steps. First, all masses were measured using a Mettler Toledo AB265-S/FACT precision balance and all silicon cantilever widths were measured using the SWLI. Second, the tee was bonded to the cantilever to be tested and then measured using the SWLI to determine its actual orientation. Masses were selected to cover a range of deformations without overloading the cantilever (overloading indicates cantilever deformations where insufficient light was reflected back to the detector or the cantilever was at risk of breaking). Third, for each mass, the base of the silicon cantilevers was leveled to the SWLI coordinate system using the interference fringes and tip/tilt stages, a measurement was completed to record the deformation, the mass was unloaded, and a final measurement was completed for the unloaded condition. These two measurements were differenced to isolate the deformation caused by mass loading from deformation that already existed, such as from the load of the tee, for example. Fourth, after all measurements were complete, the wafer was placed on a microscope glass slide and the silicon wafer thickness was measured using the SWLI. Since this step was often destructive, it was completed in only a few locations on the wafer and a mean thickness was obtained. This value was assumed for all cantilevers.

4. Force measurement results

4.1. Normal force loading

An initial experiment was performed which isolated the load to one component, F. Cantilever 2 from table 1 was mass loaded at the center hole on the tee. Eight masses (3.260, 5.426, 7.552, 9.734, 11.877, 14.059, 16.122, and 18.285 g) were individually applied to the cantilever with five trials per mass. The coefficient matrix was determined using (18) and the force was computed using (13). Note that this force prediction does not depend on the force location, measurement location, or cantilever length. The force value was converted to mass by assuming a gravity constant of 9.81 m s^{-2}. The results are presented in figure 6, where the error bars are based on the uncertainty analysis (section 4.4) with a coverage factor of 2 (95% level of confidence). The calculated mass (from the deformation measurement) underpredicts the measured mass by a mean of 6.2%, but is within the error bars. Note that the apparent parabolic trend in the data was not observed in any other tests.

4.2. Torsion force loading

All cantilevers in table 1 were loaded with at least three different masses five times per mass for each offset hole on the

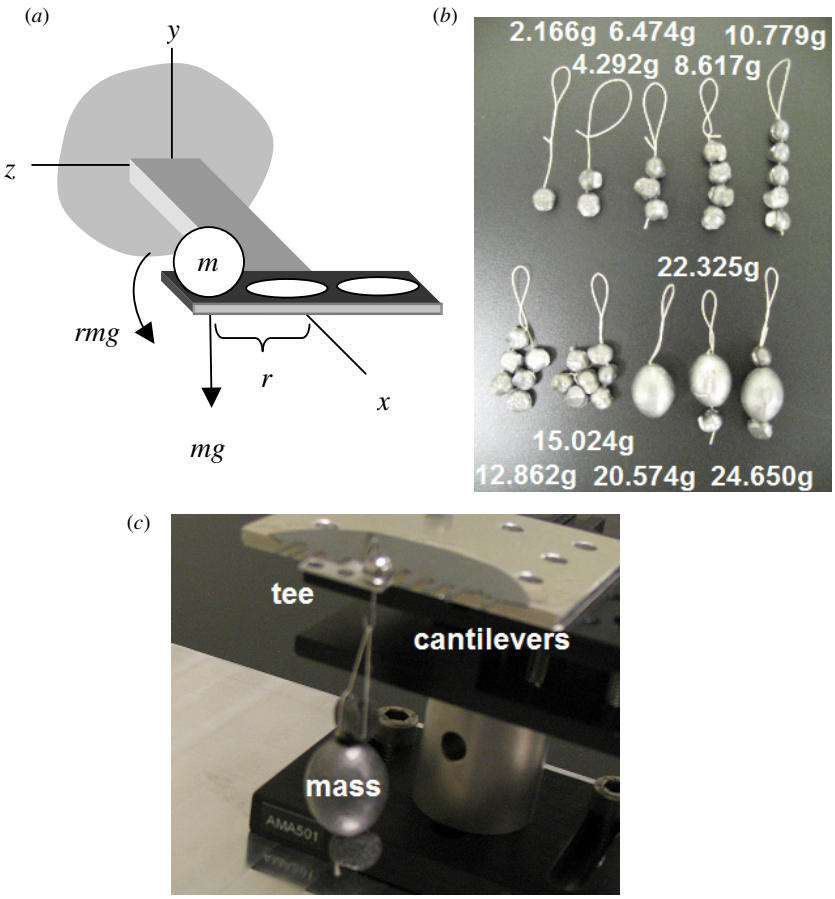

Figure 5. 'Tee' attached to cantilever: (*a*) attaching a 'tee' to the cantilever enabled offset loading, (*b*) the lead masses used to load the cantilevers are pictured, and (*c*) an array of cantilevers with one cantilever being loaded using the 'tee'.

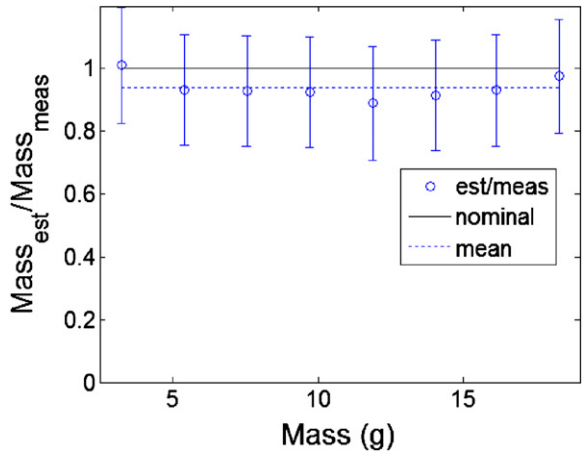

Figure 6. Normal force results for eight masses using the deformation analysis. The error bars are based on the uncertainty analysis provided in section 4.4 with a coverage factor of 2.

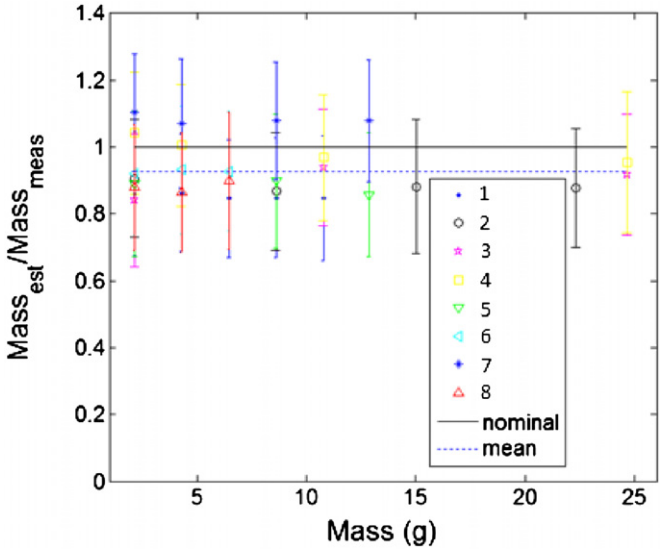

Figure 7. Torsion results when the mass was loaded at the positive torque arm. The error bars are based on the uncertainty analysis provided in section 4.4 with a coverage factor of 2.

tee. The first mass was the smallest in the set (2.166 g). The third was the largest mass the cantilever could accept without causing overloading. The other masses were selected to be between these two. The coefficient matrix was determined; the force was then computed using (15) and converted to mass as before. The results for positive torque and negative torque are shown in figures 7 and 8, respectively. Again, the predictions depend only on the local deformation of the cantilever beam measured using the SWLI. The calculated mass underpredicts the measured mass for positive torque loading by 7.4% and

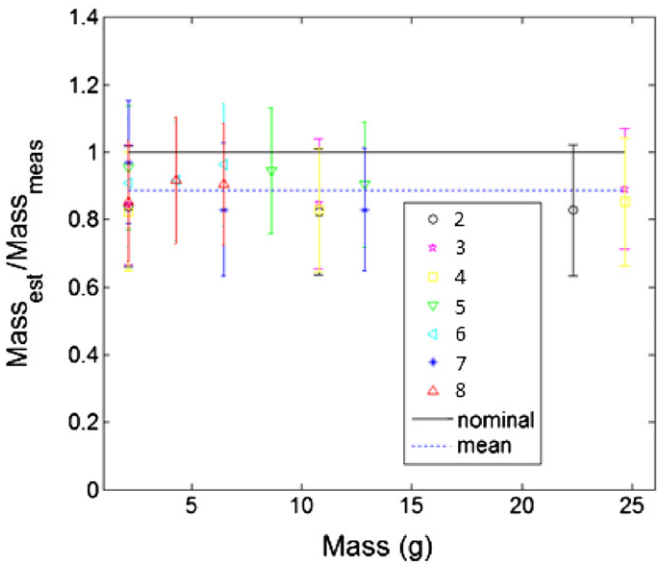

Figure 8. Torsion results when the mass was loaded at the negative torque arm. The error bars are based on the uncertainty analysis provided in section 4.4 with a coverage factor of 2.

underpredicts the measured mass for negative torque loading by 11.2%. The mean of the two results is 9.3%.

4.3. Simultaneous torsion and normal force loading

There was significant environmental noise present in the first torsion study (section 4.2) which prevented meaningful calculation of the normal force component, F, from this data. Therefore, two alterations to the setup were implemented. First, foam insulation was placed around the work area to block air currents. Second, the tethers for the masses were replaced by a rigid, stainless steel link. Motion at the mass became rigidly linked to the ball causing it to rock in its socket and transients were quickly damped. Cantilever 2 was then loaded with five masses (3.260, 5.426, 7.552, 16.122, and 18.285 g), which were applied at both offset holes (the positive and negative torque arms were 5.464 and 5.515 mm, respectively) with five trials per mass. The coefficient matrix was calculated and the mass was estimated using both normal force, by (13), and torsion force, using (15). The normal force results are displayed in figure 9 (two calculations, one for each hole) and the torsion force results are shown in figure 10 (similarly, two calculations were necessary). As before, the error bars are based on the uncertainty analysis in section 4.4 with a coverage factor of 2. The mean estimated mass using the normal force underpredicted the measured mass by 8.0% and the mean estimated mass using the torsion force underpredicted the measured mass by 11.9% (mean positive torque arm of 12.5% and mean negative torque arm of 11.2%).

4.4. Uncertainty analysis

The measurement uncertainty was evaluated using 'propagation of errors' and assuming that the covariances were zero.

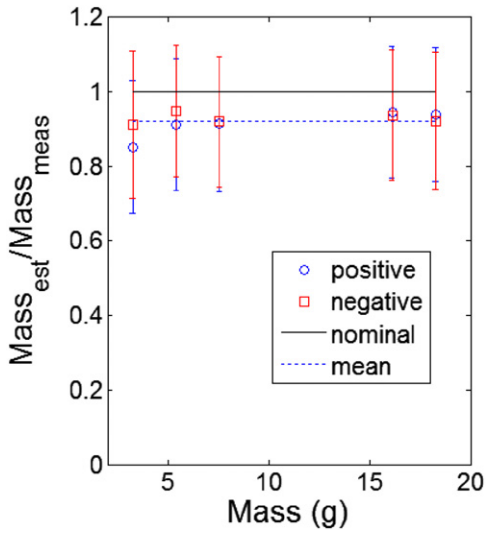

Figure 9. Normal loading results for positive and negative torque arm mass loading.

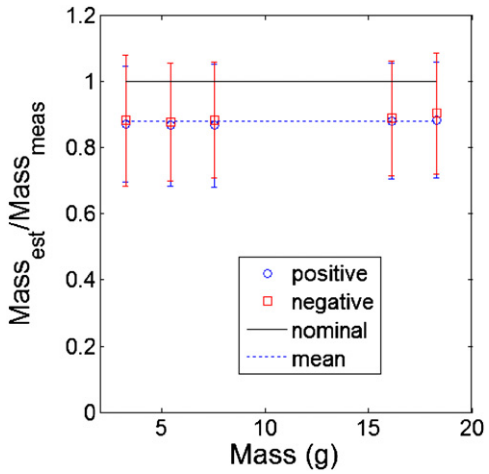

Figure 10. Torsion loading results for positive and negative torque arm mass loading.

The measurement uncertainty formula for results based on normal loading is

$$\left(\frac{\frac{\sigma_{m_{\text{est}}}}{m_{\text{meas}}}}{\frac{m_{\text{est}}}{m_{\text{meas}}}}\right)_{\text{normal}} = \sqrt{\left(\frac{\sigma_{E_{\langle 1\,1\,0\rangle}}}{E_{\langle 1\,1\,0\rangle}}\right)^2 + \left(\frac{\sigma_I}{I}\right)_*^2 + \left(\frac{\sigma_{B_3}}{B_3}\right)_*^2 + \left(\frac{\sigma_g}{g}\right)^2 + \left(\frac{\sigma_{m_{\text{meas}}}}{m_{\text{meas}}}\right)^2} \tag{19}$$

and the formula for results based on torsion loading is

$$\left(\frac{\frac{\sigma_{m_{\text{est}}}}{m_{\text{meas}}}}{\frac{m_{\text{est}}}{m_{\text{meas}}}}\right)_{\text{torsion}} = \sqrt{\left(\frac{\sigma_G}{G}\right)^2 + \left(\frac{\sigma_J}{J}\right)_*^2 + \left(\frac{\sigma_{B_1}}{B_1}\right)_*^2 + \left(\frac{\sigma_g}{g}\right)^2 + \left(\frac{\sigma_r}{r}\right)_*^2 + \left(\frac{\sigma_{m_{\text{meas}}}}{m_{\text{meas}}}\right)^2}. \tag{20}$$

Table 2. Rank-ordered uncertainty contributors.

Input	Ratio	Value
Thickness (std)	$\left(\frac{\sigma_t}{t}\right)_{\text{std}}$	3×10^{-2}
Normal force coefficient (std)	$\left(\frac{\sigma_{B_3}}{B_3}\right)_{\text{std}}$	2×10^{-2}
Torsional force coefficient (std)	$\left(\frac{\sigma_{B_1}}{B_1}\right)_{\text{std}}$	2×10^{-2}
Torque arm (align)	$\left(\frac{\sigma_r}{r}\right)_{\text{align}}$	2×10^{-2}
Shear modulus	$\left(\frac{\sigma_G}{G}\right)$	1×10^{-2}
Width	$\left(\frac{\sigma_w}{w}\right)$	3×10^{-3}–1×10^{-2}
Elastic modulus	$\left(\frac{\sigma_E}{E}\right)$	5×10^{-3}
Normal force coefficient (ls)	$\left(\frac{\sigma_{B_3}}{B_3}\right)_{\text{ls}}$	5×10^{-3}
Gravity	$\left(\frac{\sigma_g}{g}\right)$	4×10^{-3}
Torque arm (res)	$\left(\frac{\sigma_r}{r}\right)_{\text{res}}$	2×10^{-3}
Torsional force coefficient (ls)	$\left(\frac{\sigma_{B_1}}{B_1}\right)_{\text{ls}}$	2×10^{-4}
Mass measurement	$\left(\frac{\sigma_{m_{\text{meas}}}}{m_{\text{meas}}}\right)$	2×10^{-4}
Thickness (res)	$\left(\frac{\sigma_t}{t}\right)_{\text{res}}$	2×10^{-5}

In (19) and (20), the terms with asterisks were expanded further. The terms including I and J were expanded to

$$\frac{\sigma_I}{I} = \frac{\sigma_J}{J} = \sqrt{\left(\frac{\sigma_w}{w}\right)^2 + \left(3\frac{\sigma_t}{t}\right)^2_*} \tag{21}$$

with

$$\frac{\sigma_t}{t} = \sqrt{\left(\frac{\sigma_t}{t}\right)^2_{\text{res}} + \left(\frac{\sigma_t}{t}\right)^2_{\text{std}}}, \tag{22}$$

where w is the beam width, t is the beam thickness, res is associated with the SWLI height measurement resolution, and std is based on the standard deviation of thickness measurements at multiple locations on the beam. The terms including B_3 and B_1 were expanded to

$$\frac{\sigma_{B_3}}{B_3} = \sqrt{\left(\frac{\sigma_{B_3}}{B_3}\right)^2_{\text{ls}} + \left(\frac{\sigma_{B_3}}{B_3}\right)^2_{\text{std}}} \tag{23}$$

$$\frac{\sigma_{B_1}}{B_1} = \sqrt{\left(\frac{\sigma_{B_1}}{B_1}\right)^2_{\text{ls}} + \left(\frac{\sigma_{B_1}}{B_1}\right)^2_{\text{std}}}, \tag{24}$$

where the ls term is associated with the covariance matrix obtained during least-squares fitting and the std term is based on the standard deviation of repeated trials for each mass load. The term including the torque arm, r, was expanded to

$$\frac{\sigma_r}{r} = \sqrt{\left(\frac{\sigma_r}{r}\right)^2_{\text{res}} + \left(\frac{\sigma_r}{r}\right)^2_{\text{align}}}, \tag{25}$$

where res is associated with the SWLI lateral measurement resolution and align is associated with the extrapolation of the hole location using the alignment grooves instead of a stitched image of the entire tee. Representative values are provided in table 2 where the largest uncertainty contributor, cantilever thickness (standard dev), is also the term that gets multiplied by 3 in (21).

The elastic modulus for single crystal silicon depends on crystal orientation in general. For (1 1 1) silicon with the cantilever beam axis on the (1 1 1) plane, the elastic modulus is independent of orientation with a value of 168.9 GPa. However, manufacturing limits prevent perfect alignment to the (1 1 1) plane. The manufacturer-specified alignment tolerance to the (1 1 1) plane was $\pm 0.5^\circ$. Using the stiffness tensor for silicon and applying tensor rotations, the maximum uncertainty in modulus for wafer misalignment was determined to be 0.5% of 168.9 GPa.

A similar process was used to determine the uncertainty for shear modulus due to misalignment to the (1 1 1) plane. However, shear modulus does depend on the orientation of the beam axis on the (1 1 1) plane. The beam axis was nominally oriented along the [−1 −1 2] direction by cutting perpendicular to the wafer flat (the wafer flat was along the [1 −1 0] direction). The flat had a tolerance of $\pm 1^\circ$ to the [1 −1 0] direction and the cutting process had an uncertainty of $\pm 2^\circ$. Finally, the bulk shear modulus depended on the width-to-thickness ratio of the cantilever. The combined uncertainty for shear modulus was less than 1% of the nominal shear modulus (54 GPa $\leqslant G \leqslant$ 64.7 GPa).

The cantilever width uncertainty was specified as two times the SWLI lateral resolution for the selected magnification ($2(4.4) = 8.8$ μm). Dividing by the cantilever width gives a range from 0.3% to 1.3%. Similarly, cantilever thickness uncertainty was specified as two times the SWLI vertical resolution ($2(2.7) = 5.4$ nm) which was negligible for a thickness of 311 μm. However, thickness had a much greater variability when measuring at multiple locations on the same cantilever. Thickness measurements were made by placing a glass slide under the cantilever and measuring from the top of the glass to the top of the cantilever surface. This distance was affected by contaminants between the glass and cantilever and by variability in wafer thickness. Also, the setup required for measuring the thickness risked damaging the cantilevers. Therefore, a maximum variability of 9 μm was assumed based on multiple measurements of a few cantilevers at different locations on each cantilever. For a 311 μm thick cantilever, the uncertainty was 3%.

The coefficient matrix was obtained from a least-squares fit to the three-dimensional deformation data, i.e. a series of (x, y, z) points. The uncertainty in the deformation data is related to the uncertainty in the coefficient matrix by the covariance matrix. Rewriting (16) more generally,

$$y(x,z) = B_3 f_1(x,z) + H_1 f_2(x,z) + H_2 f_3(x,z) + H_3 f_4(x,z) + H_4 f_5(x,z) + B_1 f_6(x,z), \tag{26}$$

a new symmetric matrix, α, can be defined with elements

$$\alpha_{lk} = \sum_{i=1}^{n}\sum_{j=1}^{m}\left[\frac{1}{\sigma_{ij}} f_l(x_i, z_j) f_k(x_i, z_j)\right], \tag{27}$$

where l and k are the row and column numbers of α, respectively, and vary from 1 to 6, m is the number of measurements across the width of the cantilever, n is the number of measurements down the length of the cantilever, and $n \times m$ is the total number of measurements. Since measurements are obtained from the SWLI camera data, each (x, z) location is a different pixel, where i and j are the pixel indices. The term σ_{ij} is the y-coordinate measurement

uncertainty at a given pixel (i, j) and was assumed to be the same for all pixels. This enabled σ to be estimated by

$$\sigma^2 \cong \frac{1}{N-6}\sum_{i=1}^{n}\sum_{j=1}^{m}\left[y_{ij} - \left(B_3 x_i^3 + H_1 x_i^2 + H_2 x_i + H_3 z_j + H_4 + B_1 x_i z_j\right)\right]^2, \tag{28}$$

where $N = n \times m$ and 6 corresponds to the number of free parameters (the coefficients). The covariance matrix is the inverse of α. The elements of the covariance matrix are the variances and covariances of the fitted coefficients:

$$\alpha^{-1} = \begin{bmatrix} \sigma_{B_3}^2 & \sigma_{B_3}\sigma_{H_1} & \sigma_{B_3}\sigma_{H_2} & \sigma_{B_3}\sigma_{H_3} & \sigma_{B_3}\sigma_{H_4} & \sigma_{B_3}\sigma_{B_1} \\ \cdot & \sigma_{H_1}^2 & \sigma_{H_1}\sigma_{H_2} & \sigma_{H_1}\sigma_{H_3} & \sigma_{H_1}\sigma_{H_4} & \sigma_{H_1}\sigma_{B_1} \\ \cdot & \cdot & \sigma_{H_2}^2 & \sigma_{H_2}\sigma_{H_3} & \sigma_{H_2}\sigma_{H_4} & \sigma_{H_2}\sigma_{B_1} \\ \cdot & \cdot & \cdot & \sigma_{H_3}^2 & \sigma_{H_3}\sigma_{H_4} & \sigma_{H_3}\sigma_{B_1} \\ \cdot & \text{sym} & \cdot & \cdot & \sigma_{H_4}^2 & \sigma_{H_4}\sigma_{B_1} \\ \cdot & \cdot & \cdot & \cdot & \cdot & \sigma_{B_1}^2 \end{bmatrix}. \tag{29}$$

A typical result of the covariance matrix using torsion loading of 7.552 g on cantilever 2 for the positive torque arm is

$$\alpha^{-1} = \begin{bmatrix} 816.1 & -3.456 & 0.004 & 0.000 & 0.000 & 0.001 \\ \cdot & 0.015 & 0.000 & 0.000 & 0.000 & 0.000 \\ \cdot & \cdot & 0.000 & 0.000 & 0.000 & 0.000 \\ \cdot & \cdot & \cdot & 0.000 & 0.000 & 0.000 \\ \cdot & \text{sym} & \cdot & \cdot & 0.000 & 0.000 \\ \cdot & \cdot & \cdot & \cdot & \cdot & 0.001 \end{bmatrix} \times 10^{-5}, \tag{30}$$

with values for $|B_3|$ and $|B_1|$ of 18.2556 and 0.4874, respectively. Taking $\frac{\sqrt{\alpha_{11}^{-1}}}{B_3}$ and $\frac{\sqrt{\alpha_{66}^{-1}}}{B_1}$ gives uncertainties of 0.5% and 0.02%, respectively.

The coefficients also had measurement-to-measurement deviation when loaded with the same mass multiple times. Therefore, the standard deviation was computed for every measurement sequence and found to be around 2% of the mean for both B_3 and B_1. Gravity was assumed to be 9.81 m s^{-2}, but alignment to gravity was not checked so a conservative 5° deviation was assumed leading to an uncertainty of 0.4% of 9.81 m s^{-2}. The torque arms were assigned an uncertainty of two times the SWLI lateral resolution (2(4.4) = 8.8 μm). Additionally, the alignment grooves were used to extrapolate the torque arm distance. By using the extrapolation procedure and comparing to a direct measurement of the torque arm by stitching multiple images together, it was found that the torque arm could differ by as much as 100 μm, so the uncertainty was set to this limit. Finally, all masses were weighed by a precision balance with a resolution of 0.1 mg. Based on measurements performed using calibrated masses, the mass uncertainty was set to two parts in 10^4.

5. Discussion

All results underpredicted the measured mass (from 6% to 12%). The thickness was the largest uncertainty contributor at 3% (see table 2) providing a 9% uncertainty in the estimated mass compared to the measured mass. This uncertainty level is of the same order as the underpredictions (bias). It is therefore reasonable to conclude that the (single) thickness value used for all I and J calculations in (13) and (15) for normal force and torque, respectively, was too small. Thickness measurement is a significant challenge that is not unique to this research. Not only is it difficult to measure, but its uncertainty is also amplified because it is cubed in the force equation.

For the first torsion study (see the parameters provided in table 1), the estimated mass was systematically higher for the positive torque arm than for the negative torque arm (figures 7 and 8). This is contrasted with the second torsion study where the opposite trend was observed (figure 10). The reason for the difference is the method for computing the torque arms. In the first torsion study, because many cantilevers were tested, the torque arms were extrapolated based on the alignment groove. In the second torsion study, the torque arms were directly measured by stitching multiple images together to obtain both the tee and cantilever in a single view. Note that in the first study, the gap between the mean positive torque arm and the mean negative torque arm was 3.8%, while in the second study, the gap was 1.3% and in the opposite direction (total difference of 5.1%). The torque arm concept used in this research is analogous to AFM tip height. Determining these values is a significant challenge in cantilever force research.

In the study where the normal force and torsion force coefficients (figures 9 and 10) were computed from a single test, the estimated mass using the normal force could be directly compared to the estimated mass from the torsion force. The two results both underpredicted the measured mass, but by different amounts. The normal force underpredicted by 8% and the torsion force by 11.9% (difference of 3.9%). Common parameters in the force equations contribute equally and in the same direction to both results. Therefore, the difference must be because of uncommon parameters. For example, shear modulus uncertainty does not contribute to the normal force result, but does contribute to the torsion force result.

Within the framework of AFM cantilever calibration, the applicability of the force prediction approach presented here to direct and/or geometric calibration should be considered. In direct calibration, a known load is applied to set the model parameters. For geometric calibration, accurate measurements of the beam cross-section and material properties (or some equivalent representation) are required. For the direct calibration case, if it was desired to remove the biases in figures 6 through 10, one approach could be to modify the silicon wafer thickness, which (as noted) imposes the largest uncertainty in the force model. For figure 6 (cantilever 2, table 1), the bias between the mean and nominal values would be removed if the thickness was changed from 311 to 317.7 μm (this is within the 3% uncertainty level specified in section 4.4). To generalize this approach, the EI term in (13) could be treated as a single variable that is directly calibrated. This eliminates the thickness measurement challenges faced here.

For figures 7 and 8, a new thickness of 321.3 μm would remove the combined mean bias of 9.3%. Note that (1) each cantilever likely has a slightly different thickness, so the corrected value is an effective thickness for the population, and (2) this thickness is slightly outside the 95% level of confidence uncertainty range (311 μm + 0.03 × 311 μm =

320.3 μm). For figure 9, a thickness of 319.8 μm would be required for bias removal. These results are again for cantilever 2; the agreement with figure 6 thickness for bias correction is reasonable (1.8%) and within the measurement-to-measurement noise. For figure 10, based on the mean torsion force result, the new thickness would be 324.4 μm. There is a 3.9% difference between the mean normal force result (figure 9) and mean torsion force result (figure 10). Aside from measurement-to-measurement noise, all terms are the same, except for (1) the torque arm, which is not present in the normal force equation, (2) the modulus term (shear, G, or elastic, E), and (3) the torsional rigidity, J, versus the moment of inertia, I. Given that thickness alone cannot explain the discrepancy between the normal and torsional results, it is believed that the torque arm and shear modulus are also contributors in this case.

6. Conclusions and future work

Measuring the deflection of an AFM cantilever at a single spatial point requires the use of a scalar stiffness as the force transduction constant. Stiffness, however, is a poorly defined quantity for a cantilever sensing an unknown three-dimensional force vector. If, instead, deflection of the cantilever is measured at multiple points simultaneously, the force vector can be determined unambiguously. Measurements made this way are immune to many of the problems associated with traditional single-point measuring schemes. There is no dependence on where the load is applied or what portion of the cantilever is measured and there is no cubic dependence of measurement location on cantilever length. Each force component can be independently determined, whereas in single-point techniques, the total force vector must be decomposed using prior knowledge about the relationships between the force components or additional measurements must be performed.

Using a SWLI, the full-field deflection profile of rectangular cantilevers under load was measured. Masses were applied to macro-scale single crystal silicon cantilevers to cause bending and torsion. From the three-dimensional deformation, the masses were calculated and compared to an independent measurement by a precision mass balance.

There are many follow-on research topics to this study. An obvious extension is to validate the model for the third force component, P. The complete force model should also be verified using AFM-scale cantilevers. The challenge for micrometer-scale cantilevers is identifying sources of suitably small reference forces (dead weight loading becomes challenging at this scale) and determining the material properties and the thickness of multi-layered cantilevers. Another research topic could be to reduce the SWLI measurement time (the system used in this study had a measurement rate on the order of seconds). Adapting the SWLI for shorter measurement times or selecting an alternative measurement approach could reduce dynamic disturbances such as vibrations. Using a high-speed detector would also enable investigation of a dynamic three-dimensional force model. Finally, the application of this force prediction approach to direct calibration was discussed. In either direct or geometric calibration, the model simplicity and its inherent advantages (no cross-talk between torsion and normal force components and independence of the load application point and cantilever beam length) suggest that it could be applied to realize improved calibration accuracy if the three-dimensional deformation information was collected.

Acknowledgments

This work was partially supported by the National Institute of Standards and Technology. Any opinions, findings, and conclusions or recommendations expressed in this material are those of the authors and do not necessarily reflect the views of this agency.

References

Bornschlog T and Rief M 2008 Single-molecule dynamics of mechanical coiled-coil unzipping *Langmuir* **24** 1338
Brockwell D 2007 Probing the mechanical stability of proteins using the atomic force microscope *Biochem. Soc. Trans.* **35** 1564
Butt H, Cappella B and Kapple M 2005 Force measurements with the atomic force microscope: technique, interpretation and applications *Surf. Sci. Rep.* **59** 1
Butt H and Kappl M 2009 Normal capillary forces *Adv. Colloid Interface Sci.* **146** 48
Custance O, Perez R and Morita S 2009 Atomic force microscopy as a tool for atom manipulation *Nat. Nanotechnol.* **4** 803
Edwards S, Ducker W and Sader J 2008 Influence of atomic force microscope cantilever tilt and induced torque on force measurements *Appl. Phys.* **103** 064513
Emerson R and Camesano T 2006 On the importance of precise calibration techniques for an atomic force microscope *Ultramicroscopy* **106** 413
Franz C and Puech P 2008 Atomic force microscopy: a versatile tool for studying cell morphology, adhesion and mechanics *Cell. Mol. Bioeng.* **1** 4
Heim L, Kappl M and Butt H 2004 Tilt of atomic force microscope cantilevers: effect on spring constant and adhesion measurements *Langmuir* **20** 2760
Hutter J 2005 Comment on tilt of atomic force microscopy cantilevers: effect on spring constant and adhesion measurements *Langmuir* **21** 2630
Kalb J, Spaepen F and Wuttig M 2004 Atomic force microscopy measurements of crystal nucleation and growth rates in thin films of amorphous Te alloys *Appl. Phys. Lett.* **84** 25
Karhu E, Gooyers M and Hutter J 2009 Quantitative friction-force measurement by longitudinal atomic force microscope imaging *Langmuir* **25** 6203
Kim M and Pratt J 2010 SI traceability: current status and future trends for forces below 10 micronewtons *Measurement* **43** 169
Kopycinska-Müller M, Geiss R and Hurley D 2006 Contact mechanics and tip shape in AFM-based nanomechanical measurements *Ultramicroscopy* **106** 466
Langlois E, Shaw G, Kramar J, Pratt J and Hurley D 2007 Spring constant calibration of atomic force microscopy cantilevers with a piezosensor transfer standard *Rev. Sci. Instrum.* **78** 093705
Ling X, Butt H and Kappl M 2007 Quantitative measurement of friction between single microspheres by friction force microscopy *Langmuir* **23** 8392
Liu H and Bhushan B 2004 Nanotribological characterization of digital micromirror devices using an atomic force microscope *Ultramicroscopy* **100** 391

Matei G, Thoreson E, Pratt J, Newell D and Burnham N 2006 Precision and accuracy of thermal calibration of atomic force microscopy cantilevers *Rev. Sci. Instrum.* **77** 083703

McSkimin H and Andreatch P Jr 1964 Measurement of third-order moduli of silicon and germanium *Appl. Phys.* **35** 3312

Ogletree D, Carpick W and Salmeron M 1996 Calibration of frictional forces in atomic force microscopy *Rev. Sci. Instrum.* **67** 9

Rosa L and Liang J 2009 Atomic force microscope nanolithography: dip-pen, nanoshaving, nanografting, tapping mode, electrochemical and thermal nanolithography *J. Phys.: Condens. Matter* **21** 483001

Sarid D, Hunt J, Workman R, Yao X and Peterson C 1998 The role of adhesion in tapping-mode atomic force microscopy *Appl. Phys.* A **66** S283

Srinath L 1980 *Advanced Mechanics of Solids* (New Delhi: Tata McGraw-Hill) pp 239–41

VanLandingham M, McKnight S, Palmese G, Elings J, Huang X, Bogetti T, Eduljee R and Gillespie J 1997 Nanoscale indentation of polymer systems using the atomic force microscope *Adhesion* **64** 31

Veerapandian M and Yun K 2009 Study of atomic force microscopy in pharmaceutical and biopharmaceutical interactions—a mini review *Curr. Pharm. Anal.* **5** 3

Vettiger P *et al* 2002 The 'millipede'—nanotechnology entering data storage *IEEE Trans. Nanotechnol.* **1** 39–55

Wang F 2009 Comment on Influence of atomic force microscope cantilever tilt and induced torque on force measurements *Appl. Phys.* **106** 096103

Wortman J and Evans R 1965 Young's modulus, shear modulus, and Poisson's ratio in silicon and germanium *Appl. Phys.* **36** 153